A Screening Methodology for Passive Microwave Precipitation Retrieval Algorithms

RALPH R. FERRARO

NOAA/NESDIS Office of Research and Applications, Camp Springs, Maryland

ERIC A. SMITH

The Florida State University, Tallahassee, Florida

WESLEY BERG

NOAA/CIRES, Boulder, Colorado

GEORGE J. HUFFMAN

SSAI, NASA/GSFC Laboratory for Atmospheres, Greenbelt, Maryland

(Manuscript received 29 February 1996, in final form 20 November 1996)

ABSTRACT

The success of any passive microwave precipitation retrieval algorithm relies on the proper identification of rain areas and the elimination of surface areas that produce a signature similar to that of precipitation. A discussion on the impact of and on methods that identify areas of rain, snow cover, deserts, and semiarid conditions over land, and rain, sea ice, strong surface winds, and clear, calm conditions over ocean, are presented. Additional artifacts caused by coastlines and Special Sensor Microwave/Imager data errors are also discussed, and methods to alleviate their impact are presented. The strengths and weaknesses of the ''screening'' techniques are examined through application on various case studies used in the WetNet PIP-2. Finally, a methodology to develop a set of screens for use as a common rainfall indicator for the intercomparison of the wide variety of algorithms submitted to PIP-2 is described.

1. Introduction

For almost a decade, the passive sensing of upwelling microwave radiation by Special Sensor Microwave/Imager (SSM/I) radiometers has been recognized as a promising source of measurements for the estimation of precipitation. However, experience shows that the detection or ''screening'' out of nonraining pixels is generally required to obtain meaningful results, especially when performing over-land retrievals. In this context, screening consists of some type of physical, empirical, or mixed physical–empirical front-end algorithm, designed to discriminate the presence of rain from the background surface. The various rainfall intercomparison projects, including the Algorithm Intercomparison Projects (AIPs) sponsored by the Global Precipitation Climatology Project (GPCP) (see Arkin and Xie 1994) and the National Aeronautic and Space Administration (NASA) WetNet Precipitation Intercomparison Projects (PIPs) (Barrett et al. 1994a), are revealing that the advantages of rainfall retrieval measurements from the SSM/I can be offset by surface artifacts in the rain signatures, particularly over land, where the rainfall retrievals themselves are more difficult.

Although most investigators in the intercomparison projects have sought to validate the ''physics'' of their retrieval algorithms, the inability of an algorithm to identify and eliminate false rain regions, or to fail to identify all valid raining regions, can lead to the demise of an otherwise sound algorithm. It appears from the PIP-2 results (Smith et al. 1998) that on a regular basis misidentified pixels create first-order errors in the statistical comparisons of algorithms with ground-based measurements or with other algorithms. The intercomparison strategy is further complicated by the wide range in the complexity of the algorithms, with the simplest of retrieval algorithms generally being more susceptible to errors due to inadequate screening of nonraining pixels, although some of the more complex schemes are also affected. For example, correlation measures and skill scores rapidly deteriorate when there is a lack of

Corresponding author address: Ralph Ferraro, E/RA2, NOAA/NESDIS/Office of Research and Applications, 5200 Auth Road, Room 601Q, Camp Springs, MD 20746.
E-mail: rferraro@orbit.nesdis.noaa.gov

consistency between two algorithms in identifying the raining regions, even if the contributions by the disputed rain areas to the space–time averaged domain means are not significant. By the same token, when considering rain rate averages over rain-only regions, inconsistency between two algorithms in identifying the light rain areas can led to huge discrepancies in the comparisons of the means. Such discrepancies are not easily identified when making statistical comparisons between space- and time-averaged retrievals, because the errors due to screening become blurred in with the errors due to brightness temperature to rain-rate conversion. On monthly and longer timescales, even slight artifacts in a particular geographic region (e.g., coastlines, ice fields, or desert hot spots) will create persistent biases in the rainfall fields. As monthly SSM/I estimates are now routinely used by the scientific community, are an integral part of the GPCP, and have been incorporated into the AIPs and PIPs, all such applications point to the need for utilizing accurate screening techniques.

Although the most complex, physically based algorithms may include the screening step as an integral part of the precipitation retrieval algorithm (i.e., Petty 1994b), most current SSM/I algorithms are designed as a two-step process, particularly those that perform overland retrievals (see Smith et al. 1998). The first step is the rain detection (or screening step); the second is the brightness temperature to rain-rate transformation (or conversion step). The reason that it is useful to discriminate between the screening and conversion steps is that it is not uncommon for the algorithms to use different input channels, as input to the screening module, from those used for input to the conversion module. In fact, there has been a tendency for the rainfall algorithm community to address conversion as the scientific prize of the retrieval problem, relegating screening to part of the front-end engineering. Such a view has upheld a proper balance in the amount of research that has gone into the scientific nature of the screening problem, which is unfortunate since many retrieval algorithms are as vulnerable to imperfections in their screening front ends as they are to flaws in their conversion back ends. More importantly, as clear from the elegant paper by Grody (1991) on the entire problem of screening and rain detection, the physics of screening are every bit as involved as those of conversion.

In a historical sense, much of the initial SSM/I screening research was pioneered by operational agencies such as the Air Force Global Weather Central, the Fleet Numerical Meteorology and Oceanography Center (FNMOC), and the National Oceanic and Atmospheric Administration, who were concerned with generating credible, but near real time, orbit-by-orbit global rainfall patterns. Not surprisingly, the first operational screens were generally simple and formulated for computational expedience. However, these agencies are now facing a trade-off between simple computational efficient schemes, which are imperfect but adequate for global operational requirements, and more elaborate computer-intensive schemes, which more precisely discriminate rain. Recently, various studies have begun to address the ability of SSM/I algorithms to retrieve accurate climatic renditions of global rainfall; for example, see the studies of Berg and Chase (1992), Chang et al. (1993), Spencer (1993, 1994), Adler et al. (1994), Ferraro et al. (1994a), and Ferraro et al. (1996). One of the important contributions of the more recent precipitation intercomparison projects has been the recognition by SSM/I rainfall algorithm developers that, without precise screens for rain detection, such rain accumulations or rain-rate products are corrupted (especially over land), even if the space–time averages appear correct. Notably, more complex retrieval schemes become more feasible to run for both daily and climatic timescales, if nonraining pixels can be identified prior to the generally more computational intensive brightness temperature to rain-rate conversion step.

The focus of this paper is to present an analysis of various screening procedures that have been developed for use with SSM/I measurements. A comparison of different approaches will be presented, together with examples of their successes and failures. The paper concludes with the description of an approach used during PIP-2 to develop a consistent ''common screen'' for rain/no rain identification, which combines a first-guess rain identification algorithm with different types of screen discriminators for different types of background surfaces. Because of the wide range in complexity of the algorithms submitted to PIP-2, a common screen was developed and employed, and enabled the 20 different algorithms to be compared on a standardized basis, thus separating errors due to identification of rain presence from errors arising during conversion of brightness temperatures to rain rate magnitudes; see Smith et al. (1998). It should be noted that this method did limit the effectiveness of some algorithms, in particular those which perform iterative solutions to finalize the rain area and do not require front-end screens (i.e., Petty 1994b).

2. Review of microwave signatures

a. Previous studies

Over ocean, radiative transfer models can generally simulate surface and atmospheric conditions accurately on the scale of the SSM/I field of view (FOV), with most of the surface effects due to wind influences on the ocean surface (Wilheit et al. 1977). The main modeling problem over ocean is the so-called beam-filling effect due to nonlinear effects of clouds and rain in the FOV (Petty 1994a).

Over land, the complicated emissivity variations due to surface type and vegetation cover render radiative modeling of the SSM/I FOV extremely difficult. Hence, most models simulating land surface signatures have

been based upon those conditions observed from surface-based radiometers or low-flying aircraft measurements (i.e., Wigneron et al. 1993; Schmugge 1983), both of which are at much higher spatial resolution and not applicable to satellite retrievals. Ferraro et al. (1986) used *Nimbus-7* Scanning Multichannel Microwave Radiometer (SMMR) measurements at 19 and 37 GHz to classify surface type from passive microwave measurements. More recently, to meet the needs of the Department of Defense, the SSM/I Calibration/Validation team (Hollinger 1991) developed a series of rules to classify several types of surfaces (Neale et al. 1990). Other types of approaches, such as discriminant analyses, neural networks (Lure et al. 1993), and geographic databases (Conner and Petty 1996), have also been used to classify various surface types from SSM/I data.

From the standpoint of global rain identification, Grody (1991) developed the most widely used set of rules to separate rain from snow and deserts. Ferraro et al. (1994b) expanded on those ideas and developed a more expansive set of screens to be used for rainfall retrievals that included separate indicies for land and ocean, improved screens for semiarid land, coastlines, and sea ice, as well as some discussion on the uncertainties related to each screen. The basic philosophy of these approaches is to develop screens that can be used globally and to use actual SSM/I measurements to develop empirical relationships. The trade-off between the conservative nature of global screens and their limitations for regional applications will be discussed below.

b. Land signatures

Over land, the brightness temperature (TB) variations observed by the SSM/I sensor in the frequency range of 19–85 GHz are primarily controlled by the underlying surface, except when precipitating clouds are present. This is because of the rather high emissivity (ε) of the land surface. Although the atmosphere does contribute to the satellite-measured TB, its contributions are generally less than 10% of the observed variability in the absence of precipitation. Since the ε variations within an FOV can vary drastically, it is difficult to separate the atmospheric contribution from the total signal. Also, in regions of low ε (i.e., snow cover) the atmosphere is generally dry, so its contributions are again negligible. Hence, to a first-order approximation (neglecting atmospheric contributions), the satellite-measured TB over land is a product of ε and the surface temperature. Typical ε values over land range from 0.6 to 0.95 and vary with frequency and surface type (Grody 1988). Because of this high variability and because the weakest scattering rain clouds emit at temperatures that are nearly the same as the underlying surface, detection of the emission signals of cloud and rain over land is not always possible. Hence, essentially all land-based rain-retrieval algorithms utilize the scattering properties of rain, as is described below.

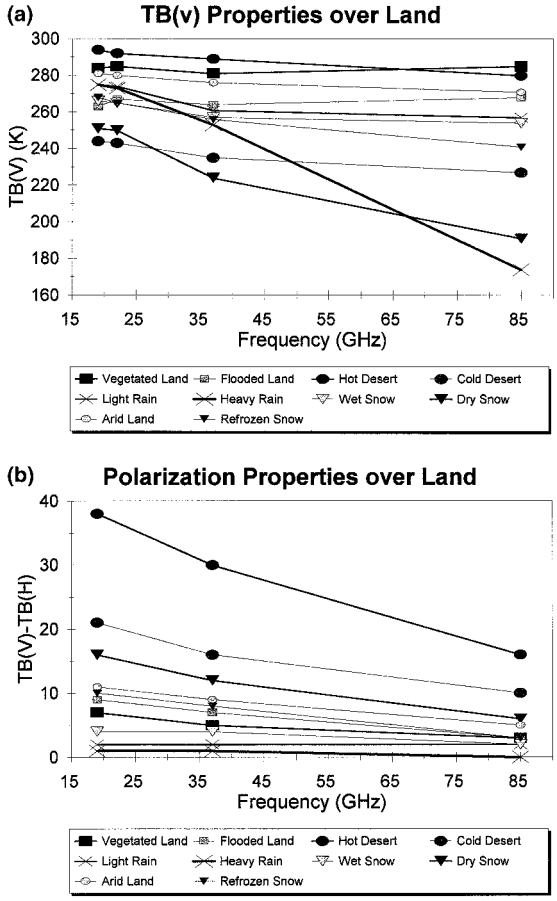

FIG. 1. Brightness temperature variations as a function of frequency for various land surface types. (a) Vertical polarization variations and (b) polarization differences.

A schematic of ''typical'' TB and polarization variations with frequency is shown in Fig. 1 for a variety of surface types. These were obtained from actual SSM/I measurements where ancillary data were available to classify the different surface types. Those surfaces that show an increase in TB with frequency are referred to as ''absorbers,'' while those which exhibit a decrease in TB with frequency are ''scatterers.'' As can be seen from Fig. 1a, there are several surface types (i.e., snow and desert) that exhibit a scattering signature that is similar to precipitation, especially light rain. In addition, there are other surface types, referred to here as ''transient'' surfaces (i.e., semiarid land and refrozen snow), that also exhibit similar signatures. All of these surfaces must be screened properly in order to identify rain in the satellite FOV. As discussed below, a decision must be made as to whether the rain rate is ''zero'' or ''indeterminate'' over these surfaces.

Polarization differences [e.g., TB(V) − TB(H)] are also a function of surface type and frequency, and these are depicted in Fig. 1b. For most of the surfaces, the polarization is greater at 19 GHz than at 85 GHz, whereas precipitation exhibits a rather flat polarization sig-

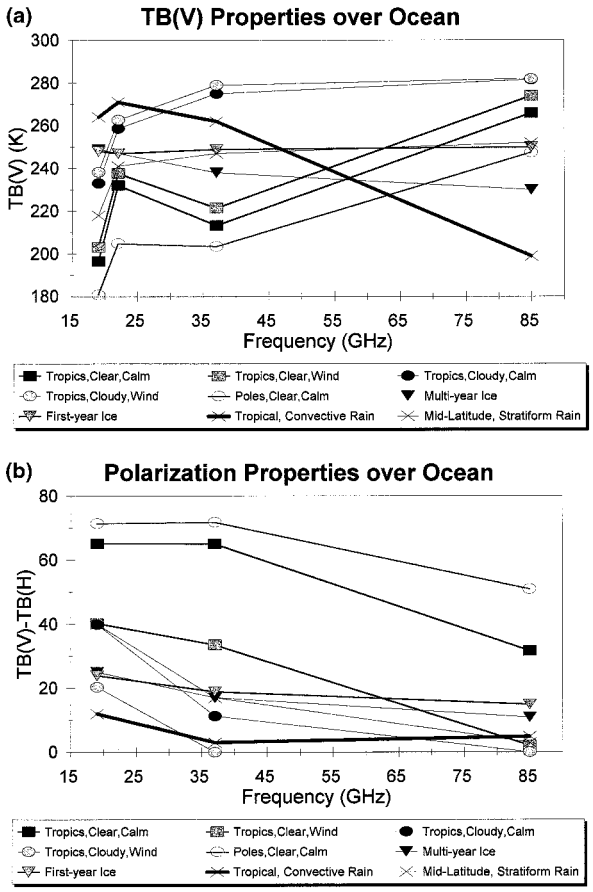

FIG. 2. As in Fig. 1, but for ocean surfaces. Wind conditions are for a speed of 30 m s^{-1}.

nature with frequency. Finally, desert surfaces generally have the highest polarizations of all the land surfaces although some snow surfaces also exhibit similar characteristics.

It is evident from Fig. 1 that simple single-channel or polarization difference thresholds cannot be used to uniquely identify the rain signature from other land surface types. As will be discussed below, both frequency and polarization information are used in the screening procedures.

c. Ocean signatures

Over ocean, the TB measured by the satellite is controlled by both the surface and the intervening atmosphere conditions. Since the ε of the ocean is low (approximately 0.5), the contributions due to clouds, water vapor, and precipitation drastically alter upwelling surface emission. Additionally, the presence of sea ice and increases in surface wind speed increase the ε. The spectral signatures of these features are shown in Fig. 2. It should be noted that these values were obtained through the use of the radiative transfer model described by Weng (1992a,b), except for the values over precipitation, which were obtained from actual SSM/I observations. Additionally, the ''wind'' conditions shown in Fig. 2 are for extremely high wind speeds (e.g., 30 m s^{-1} or greater), which are indicative of the largest possible surface effects caused by wind.

Over clear, calm oceans, the TB signature is ''cold'' and highly polarized. The influence of water vapor is to increase the TB and decreases the polarization. The values at 22 GHz show the greatest effect, since they are near the center of a weak water vapor absorption band, and the effect is greater in the Tropics than in polar regions. A weaker change occurs at 85 GHz, which is also partially influenced by water vapor. For precipitation measurements, the effect of water vapor can generally be minimized by using measurements at 22 GHz in the retrieval algorithm. The effect of strong winds will increase the TB somewhat but dramatically reduce the polarization. It should be noted that the horizontal polarizations are more sensitive to these effects, but we have chosen to show vertical polarization since this is the only orientation available at 22 GHz. The presence of nonraining clouds drastically alters the TB and polarization signatures, and is much greater than wind effects alone. The absorption due to cloud water effectively reduces the contribution from the surface and increases the TB, with the amount of the TB increase being a function of the liquid water content and cloud fraction within the satellite FOV. Light rain generally exhibits a similar signature to that of clouds. However, in heavy convective rain, a decrease in TB at 85 GHz and sometimes at 37 GHz can be seen, especially from those storms that form over land, move offshore, and exhibit characteristics similar to those found over land (Spencer et al. 1989). The sea-ice signatures exhibit some of the same TB and polarization characteristics of the other ocean signatures.

3. Screening techniques

a. Overview

There are four main classes of screens that must be used in order to generate accurate SSM/I rain retrievals. The first class will be termed ''quality control,'' which deals with the removal of unrealistic TBs (i.e., out of physical limits), calibration errors (i.e., inconsistencies from scan line to scan line), and mislocated orbits. The second class will be termed ''data corrections'' and deals with special situations where certain corrections need to be applied. The third class will be termed ''geographic'' and deals with the proper identification of nonprecipitating coastline scenes. Because the radiative response and size of the SSM/I FOVs vary with frequency, the sharp gradient at the coast can cause considerable problems in the rain retrievals, especially when different techniques are used over land and water. The final class will be termed ''surface screens'' and deals with the

proper removal of artifacts due to specific surface types. These are described in detail in the following sections.

The impact of false signatures warrants some further discussion. On the instantaneous scale, improper removal of large-scale features such as snow cover or desert will create unrealistic rain fields. Thus, the need for a surface screen will be quite obvious. However, there are typically more subtle features that will appear as a few ''noisy'' FOVs within the orbital swath. These could be caused by improper identification of coastlines or perhaps inadequate removal of snow regions. Although these may not seem like much of a problem, they will show up in the monthly mean rain field, since they may occur respectively in the same geographic region.

Before we describe the specific screens that can be used with the SSM/I, some words on the philosophy of screening are needed. There are two schools of thought regarding how screening should be used. One approach is to address screening as part of the retrieval problem, while the other is to utilize proper identification of potential rain measurements prior to the rain-rate retrieval step. Regardless of which philosophy is employed, the algorithm needs to be able to identify surfaces where rain retrievals are impossible (e.g., over snow and ice, where the rain signature cannot be uniquely separated from the surface conditions) or are unlikely (e.g., over deserts, where it rarely rains). This leads to the issue of whether an algorithm should ''dynamically'' determine nonraining pixels or whether it would be sufficient to use some sort of static surface mask, which could be based upon climatology (i.e., for snow and ice) or geography (i.e., for deserts and semiarid land). In addition, temporal variations of the SSM/I measurements may also be a viable approach (e.g., Connor and Petty 1996). A third issue is the use of global screens versus regional screens. As was previously described, there are virtually no available radiative model simulations over land that can realistically describe the signature of the SSM/I FOVs. Hence, many of the screens developed are empirical in the sense that the equations are based upon comparisons between observed precipitation and actual SSM/I measurements. Thus, these screens will be implicitly tuned to the SSM/I algorithm employing them and the observed training dataset where they originated. If the training dataset is regional, the screens will do well in that particular area of the earth but may fail badly over other geographical locations. On the other hand, if the training dataset is global, the screens may perform better over all locations but tend to show systematic errors in certain regions.

b. Quality control screens

It was discovered early on from the archive of the *F8* SSM/I antenna temperatures that mislocated and nonphysical antenna temperatures were present in the data. Because of the sensitivity of SSM/I rainfall algorithms to relatively small variations in brightness temperatures, combined with the relatively infrequent occurrence of intense rainfall events, erroneous data occasionally produce serious errors in the resulting rainfall estimates. For instantaneous scenes these erroneous rainfall rates are usually quite obvious. For climatological rainfall estimates, the skew of the rainfall distribution towards lower rainfall rates means that erroneous rainfall estimates resulting from nonphysical data may dominate the time-averaged precipitation estimates.

Three basic types of errors occur in the SSM/I data. First, large blocks of scans occasionally are mislocated by up to several thousand kilometers. This problem seems to be the result of attaching the wrong time tag to the data, which translates to an incorrect geolocation. Second, from time to time the values in an entire scan appear systematically different than the values in neighboring scans. This usually occurs for a single scan and often for only one or two channels in that scan. Such jumps appear to be the result of calibration problems. As an example, a number of these individual bad scans are manifest in several of the high-resolution monthly rainfall estimates produced for PIP-1 (Barrett et al. 1994b). The third type of error is the occurrence of nonphysical antenna temperatures for a single pixel as the result of telemetry errors.

Wentz (1992) described a technique for identifying mislocated blocks of data by seeking systematic differences between instantaneous brightness temperatures and (spatially varying) semimonthly averages of brightness temperature, channel-by-channel. A recent catalogue of these blocks, plus some known problem periods, appears in Wentz (1993).

Two different approaches have been taken to control erroneous isolated scans due to calibration errors. Wentz (1993) describes a series of checks on the SSM/I calibration data (hot counts, cold counts, etc.), providing empirically based limits to the variation in the calibration. His method had to be modified for data recorded after 9 October 1990 because the level-1 processing of SSM/I data was modified to average the calibration values over 10 scan pairs.

The other approach to identifying calibration errors involves computing scan-average antenna temperatures for each channel and throwing out scans with an average that is ''too different'' from the neighboring scans. Based on an analysis of these bad scans, Berg and Chase (1992) applied a difference threshold of 20 K for all channels. In developing the Goddard Scattering Algorithm, Version 2 (GSCAT2), Adler et al. (1994) set the thresholds 25, 22, 22, 27, 21, and 22 K for the 19H, 19V, 22V, 37H, 37V, and 85H channels, respectively. These limits were set by inspecting histograms of scan average for each channel at each pixel during June 1989. Both groups that developed the scan-average method noted that the technique does result in the very occasional discard of legitimate data when a land–ocean boundary is aligned with the scan track. While Wentz

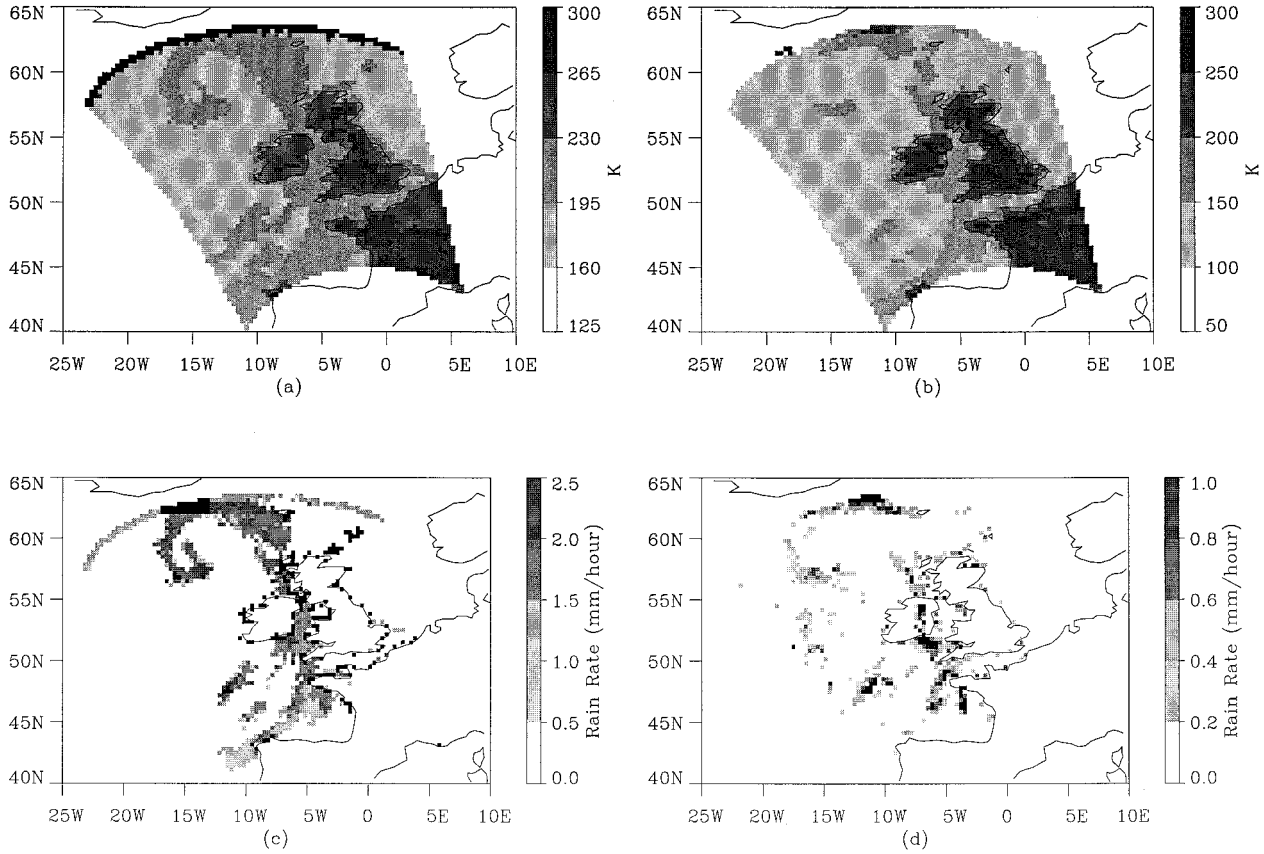

FIG. 3. Example of bad scan data for PIP-2 case 6, overpass 5 (24 November 1992, 1704 UTC). (a) 19-GHz vertical TB, (b) 19-GHz horizontal TB, (c) rain rate from the Cal/Val algorithm, and (d) rain rate from the Ferraro algorithm.

(1993) reported that his calibration checks typically flagged about 0.05% of scans, the GSCAT2 group found that their technique eliminated about 0.017% of the pixels for the period July 1987 through June 1988, with no month losing more than 0.050% of the pixels. The GSCAT2-identified scan errors are almost entirely a subset of the Wentz-identified scan errors.

Another data problem involves telemetry errors that result in nonphysical antenna temperatures. All three groups use a simple check that the antenna temperatures are within reasonable physical limits. Adler et al. (1994) used the range 50–323 K, Berg and Chase (1992) used 90–370 K, and Wentz (1991) used 55–320 K. These values represent ranges in TB that are thought to be the approximate physical limitations of measurements in the SSM/I FOV and are based on both empirical and radiative transfer calculations.

It is recognized that data mislocations between relatively similar regions or telemetry-related errors resulting in antenna temperatures within physical bounds will bias rainfall estimates. It is also important to note that both telemetry and calibration problems may not affect all seven channels, so it is necessary to apply the quality control screen to all the channels used in the retrieval algorithm.

An example of the effect of a bad scan on the resulting rainfall estimates is shown in Fig. 3 (northernmost scan). Although in this case the erroneous scan is present in all seven channels, the mean scan TB jumps from 190 to 526 K (+336 K) in the 19-GHz vertical channel but only changes from 125 to 112 K (−13 K) in the 19-GHz horizontal channel. In this case many of the 19V scan values are outside of the physical bounds as well. Figure 3 also demonstrates the variable effects this sort of error can have on different retrieval algorithms. The Cal/Val algorithm (Hollinger 1991) (Fig. 3c) shows a constant rainfall rate of around 1.5 mm h^{-1} across the scan, while the Ferraro algorithm (Fig. 3d) produces extreme rain rates at the maximum of 35 mm h^{-1} cutoff near the center of the scan.

c. Data corrections

The *F8* dataset contains periods of 85-GHz channel failures. Although this is not necessarily a quality control issue in the sense that it needs to be checked routinely, the failure to recognize these time periods will undoubtedly cause erroneous rain retrievals. Details on the channel failures are described by Hollinger (1991). By May 1988, the 85V channel becomes too noisy to

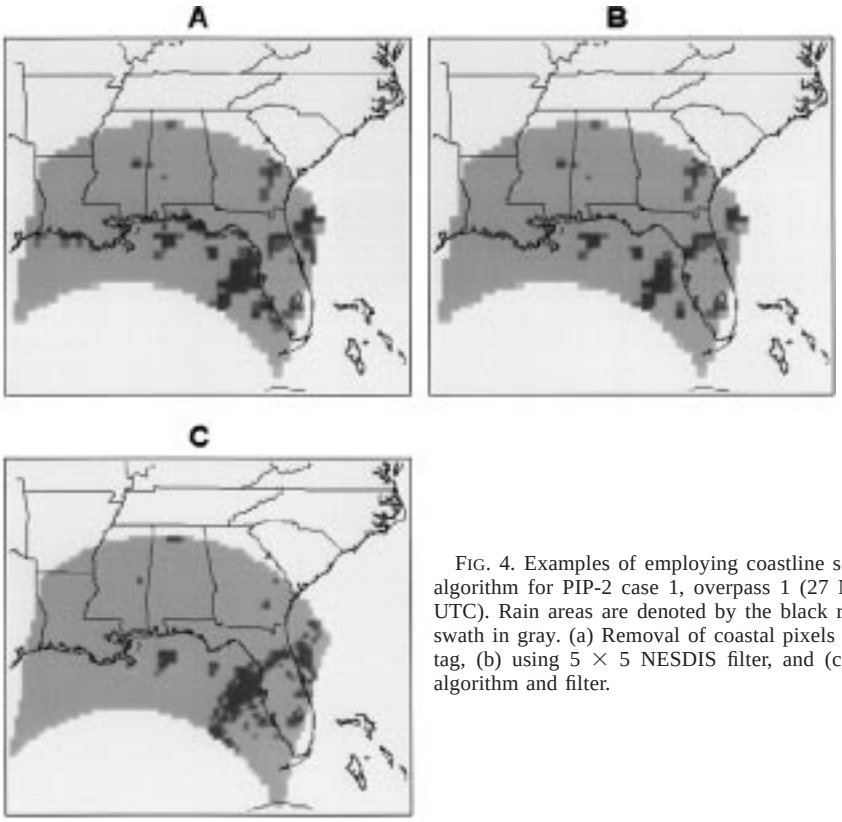

FIG. 4. Examples of employing coastline screens to the NESDIS algorithm for PIP-2 case 1, overpass 1 (27 November 1987, 0021 UTC). Rain areas are denoted by the black regions and the SSM/I swath in gray. (a) Removal of coastal pixels from FNMOC surface tag, (b) using 5 × 5 NESDIS filter, and (c) using GSCAT2 rain algorithm and filter.

be used for reliable rainfall retrieval, while the 85H channel becomes noisy after April 1990. A procedure to synthesize the 85V channel is described by Ferraro and Marks (1995) and is presently being used by the SSM/I Pathfinder Project. This routine can extend the period of usable 85V measurements for those algorithms that rely on that channel. However, since the primary predictor in the relationship is generally the 85H, algorithms relying on both polarizations during the bad data period should use the synthesized TB(85V) with caution, since it is not really an independent measurement.

Wentz (1992) has noted small, systematic differences between the planned and apparent boresight nadir angle, as well as alignment of the SSM/I sensor relative to the Defense Meteorological Satellite Program (DMSP) spacecraft. These differences result in apparent along-track and yaw errors, respectively. Corrections for these errors are described in Wentz (1992, 1993).

d. Geographic screens

Three viable options are presented here to distinguish the coastline in the SSM/I data and are illustrated in Fig. 4. The SSM/I datasets produced at FNMOC (and used as input from the Wentz dataset) has attached a surface-type tag. This tag identifies land, ocean, coast, seasonal sea ice, and perennial sea ice in each set of FOVs. The easiest method for coastline identification is to simply discard any observation tagged as coast and perform no retrievals there. However, this will eliminate raining coastal pixels. Since the SSM/I FOVs are relatively large, they contain a mixture of land and water that extends farther than one pixel from the coast and can cause false rain signatures (Fig. 4a).

A more sophisticated scheme to minimize coastline effects and employed by the National Environmental Satellite, Data and Information Systems (NESDIS) set of algorithms during PIP-2 (e.g., the Ferraro, Grody, Alishouse, and NESDIS algorithms as described in Smith et al. 1998) was to use a 5 × 5 grid of A-scan observations surrounding the pixel for which the retrieval is performed. Any coastline or land identified in this grid was classified as land. They simply used their land algorithm over these coast and ''near coast'' FOVs. This approach seems to alleviate many of the false signatures along the coastline (Fig. 4b). The trade-off for this approach is that the sensitivity to emission-type rain is lost along the coast; however, this is better than no retrieval at all. In addition, there is not much difference noted in convective rain.

The most sophisticated scheme presented here to identify nonprecipitating coastline pixels is described by Adler et al. (1993). After identifying clear-sky cold ocean [see Eq. (12)], clear-sky coast is identified as

$$\sigma[\mathrm{TA(85H)}] > 10\mathrm{K} \quad \text{and}$$
$$\rho[\mathrm{TA(37H)}, \mathrm{TA(85H)}] > 0.5 \quad \text{and}$$
$$\mathrm{slope} < 1.2, \tag{1}$$

where σ is the standard deviation, ρ is the cross correlation, and slope is defined as

$$\mathrm{slope} = \rho[\mathrm{TA(37H)}, \mathrm{TA(85H)}] \times \sigma[\mathrm{TA(85H)}] \times \sigma[(\mathrm{TA(37H)}] - 1, \tag{2}$$

all of which are computed on a 5×5 pixel array centered on the pixel of interest. These tests identify cases in which low humidity allows the (similar) surface emission signals from 37H and 85H to dominate the SSM/I signal. Adler et al. (1993) also recommend another test, run before (1) and (2), to identify cases that satisfy the coast check but proved to have precipitation in verification studies. This ''not-coast'' test diagnoses the presence of precipitation when

$$\mathrm{TA(85H)} - \mathrm{TA(37H)} \leq -10 \text{ K}. \tag{3}$$

Note the excellent continuity along the west coast of Florida (Fig. 4c).

Finally, it should be noted that the use of the polarization-corrected temperature (PCT) approach (Spencer et al. 1989) and similar procedures (Conner and Petty 1996) can also be used to minimize coastline affects. These procedures involve a linear transformation between TV and TH that effectively removes the land–ocean emissivity contrast. Care must be taken to account for variations in this relationship during different seasons and in different geographic regions.

e. Land surface screens

As was previously described, some researchers want the screening for rain–no rain pixels as a separate part of the retrieval process, while others feel that it should be part of the retrieval. Although the formulation for many of screens derived below are based upon the presence of a ''scattering signal'' (Grody 1991), the screens will be described as separate entities. Some brief discussion on how the scattering signal can be detected will also be discussed.

1) IDENTIFYING RAIN

The scattering signatures of rain (and other surfaces) can generally be detected by utilizing the decrease in TB with frequency as illustrated in Fig. 1. This signature is most easily obtained by comparing a low-frequency measurement (e.g., 19 or 22 GHz) with a high-frequency measurement (e.g., 85 GHz). Ferraro et al. (1994b) present this basic identification of scatterers as any occurrence of the TB(22V) > TB(85V). A more precise measure of scattering can be obtained using a global dataset of nonscattering measurements to generate a function called a ''scattering index'' (Grody 1991), which combines the 19-, 22-, and 85-GHz channels. The departure of this estimate from the actual measurement at 85 GHz is a measure of the scattering signal, with the potential rain areas being identified by an index value exceeding 5–10 K. Other viable methods include simple thresholds of the 85-GHz temperatures (i.e., the GSCAT2 algorithm in PIP-2), the use of the PCT methods at 37 and/or 85 GHz (see the Kidd and Spencer algorithms in this issue), and multichannel discriminant functions used in the SSM/I Cal/Val algorithm (Hollinger 1991). Another approach, which utilizes climatological TB information based upon data for a period prior to the retrievals or a similar time period from previous years is also used by some investigators (i.e., Kniveton et al. 1994; Conner and Petty 1996).

Shown in Fig. 5 are three of the approaches described above applied to a squall line over the central United States (PIP-2 case 2, overpass 1). It should be noted that no screening for nonraining pixels was applied in this example. The areas of rain depicted by the scattering index (Fig. 5a), the TB(22V) − TB(85V) ≥ 3K (Fig. 5b), and those below GSCAT2 TB(85H) threshold of 253 K (Fig. 5c) are very similar, except in the northwest portion of the region, where snow cover was present. Use of the snow screen (discussed below) will properly remove these regions. The region of rain indicated by the scattering index with the 5-K threshold and the TB(22V) − TB(85V) algorithm with a 3-K threshold both pick up some other rain regions (e.g., eastern Texas and northern Arkansas) but probably some nonraining areas as well (e.g., southeastern Alabama). This is confirmed by examining the Geostationary Operational Environmental Satellite (GOES) IR image (Fig. 5d). Clearly, higher rain/no rain thresholds than used in this example, with proper screening logic, are needed for these two approaches.

2) IDENTIFYING DESERTS

Desert surfaces are much more highly polarized than precipitation and other surfaces. Grody (1991) removed desert from the rain signature using the condition

$$\mathrm{TB(19V)} - \mathrm{TB(19H)} > 20. \tag{4}$$

The SSM/I Pathfinder algorithm (NASA 1996; denoted SSMI-PF), which is a revision of the Neale et al. (1990) and Hollinger (1991) method for desert identification is more complicated:

$$\mathrm{TB(22V)} - \mathrm{TB(19V)} \leq 4 \quad \text{and}$$
$$[\mathrm{TB(19V)} + \mathrm{TB(37V)}]/2 - [\mathrm{TB(19H)} + \mathrm{TB(37H)}]/2 \geq 19.7 \quad \text{and}$$
$$\mathrm{TB(85H)} - \mathrm{TB(37H)} > -6.2 \quad \text{and}$$
$$\mathrm{TB(19V)} > 264. \tag{5}$$

Shown in Fig. 6 is an application of both these techniques. The Grody (1991) method appears to detect a

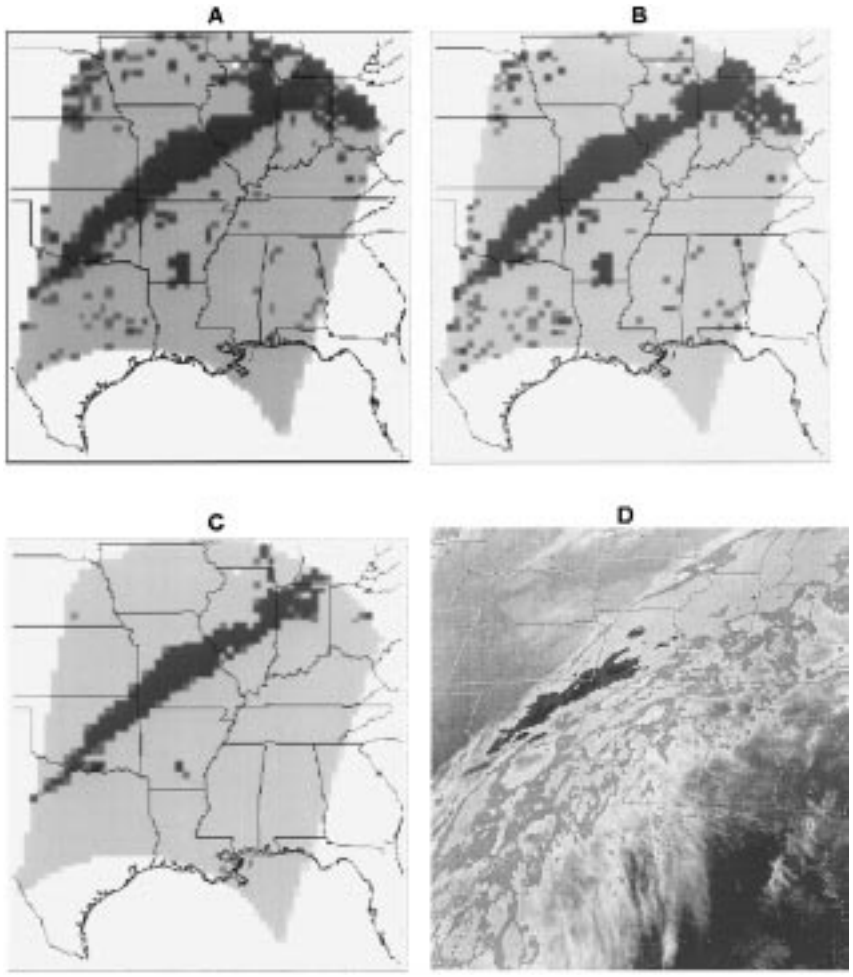

FIG. 5. Examples of rain/no rain discrimination techniques, without any screening logic, for PIP-2 case 2, overpass 1 (25 November 1987, 0044 UTC). Rain areas are denoted by the black regions and the SSM/I swath in gray. (a) Use of the scattering index with a threshold of 5 K, (b) TB(22V) − TB(85V) ≥ 3 K, and (c) TB(85H) < 253 K.

slightly larger area of desert than that found when using Eq. (5).

3) IDENTIFYING SEMIARID LAND

Arid regions, some of which prevail at high altitudes, can also produce a scattering signature. These surfaces are generally nonvegetated and consist of dry soil for a portion of the year. They exhibit strong polarization characteristics but not as strong as desert regions. An example of this type of surface is located in the Sahel region of Africa and occurs during the winter months. This portion of Africa is used for agriculture, although during the winter months there is very little rain in these regions. The exact cause for the scattering signal is unclear, although we speculate that the dry, nonvegetated soil may allow for deeper penetration of the low-frequency measurements into the soil, causing a lower temperature at 19 and 22 GHz than at 85 GHz. A check developed by Ferraro et al. (1994a), which can be used to identify and remove these features (particularly over the Sahel), is given as

$$\mathrm{TB(85V)} > 253 \quad \text{and} \quad \mathrm{TB(19V)} - \mathrm{TB(19H)} > 7. \tag{6}$$

Global application of this check can sometimes remove light rain over cold surfaces (e.g., PIP-2 case 23, overpass 2). A similar check developed for use by the GSCAT2 algorithm but that may perform better globally is given as

$$\mathrm{TB(19V)} - \mathrm{TB(19H)} > 10.25 \quad \text{and}$$
$$\mathrm{TB(19V)} - \mathrm{TB(19H)} > 0.25(301 - \mathrm{TB(85H)}). \tag{7}$$

Finally, the SSMI-PF rule for identifying semiarid land/sparse vegetation is

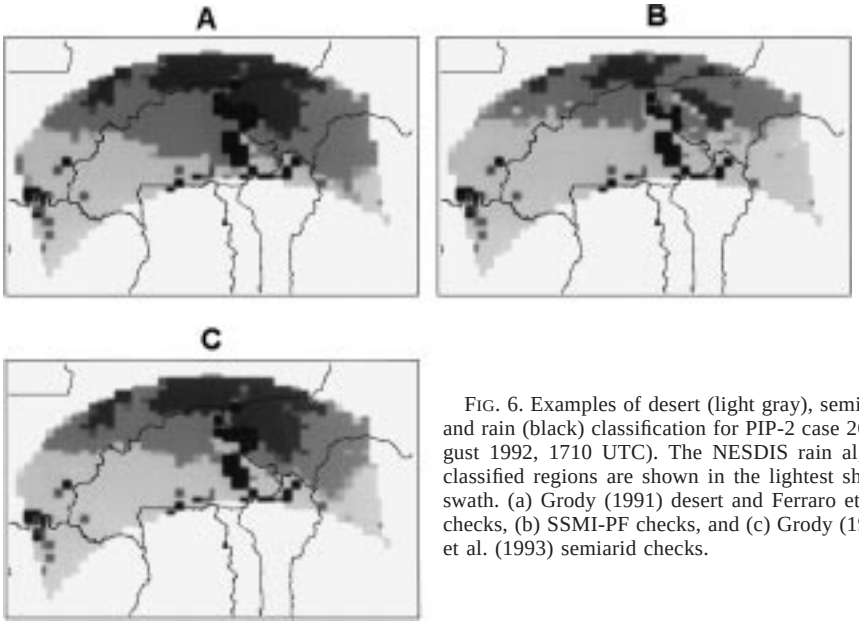

FIG. 6. Examples of desert (light gray), semiarid land (dark gray), and rain (black) classification for PIP-2 case 26, overpass 1 (28 August 1992, 1710 UTC). The NESDIS rain algorithm is used. Unclassified regions are shown in the lightest shade to denote orbital swath. (a) Grody (1991) desert and Ferraro et al. (1994b) semiarid checks, (b) SSMI-PF checks, and (c) Grody (1991) desert and Adler et al. (1993) semiarid checks.

$$\begin{aligned} \mathrm{TB(22V)} - \mathrm{TB(19V)} &\le 4 \quad \text{and} \\ 10.5 &< [\mathrm{TB(19V)} + \mathrm{TB(37V)}]/2 \\ &\quad - [\mathrm{TB(19H)} + \mathrm{TB(37H)}]/2 \\ &< 19.7 \quad \text{and} \\ \mathrm{TB(85V)} - \mathrm{TB(37V)} &< 4.2 \quad \text{and} \\ \mathrm{TB(37V)} - \mathrm{TB(19V)} &< -1.3 \quad \text{and} \\ \mathrm{TB(37V)} &> 257. \end{aligned} \tag{8}$$

Comparisons of use of these methods are shown in Fig. 6. The Grody (1991) method detects the largest area of semiarid land and the SSMI-PF the least. Interestingly, the GSCAT2 method appears to be a compromise of those two techniques.

4) IDENTIFYING SNOW COVER

As shown in Fig. 1, there are several classes of snow cover that need to be identified for proper rainfall classification. These include dry snow, wet/melting snow, and refrozen snow, all of which have different TB and polarization difference variations with frequency. Snow cover can be identified in a number of ways. Perhaps the most complex method is the dynamic retrieval of snow cover from the SSM/I observations. Grody and Basist (1996) have developed a stand alone algorithm for snow cover detection from the SSM/I. This algorithm has recently been implemented at FNMOC and has replaced the classification scheme developed by Neale et al. (1990). Since both of these techniques involve several steps and checks, they are not provided in this paper. However, both utilize the scattering and polarization signatures to identify snow and separate snow cover from other surface types. Figure 7 shows the identification of snow using these algorithms, with the remaining rain–no rain areas being determined by the NESDIS rain algorithm. The use of the Grody and Basist algorithm (Fig. 7a) delineates a much larger area of snow cover than that originally used by FNMOC (Fig. 7b). This results in some false rain signatures in northeastern Pennsylvania.

Another viable approach is to use climatological information to screen for snow cover. For example, the National Snow and Ice Data Center has developed a climatology of weekly snow cover on a 25-km grid based upon the NESDIS operational product for the period of 1978–94. This climatology contains mean snow cover, probability of occurrence, and snow cover variance. Ferraro et al. (1996) have produced a one-degree gridded monthly snow cover frequency climatology based upon the Grody and Basist (1996) algorithm for the entire SSM/I time series, which is updated monthly and archived at the National Climate Data Center (NCDC) Either of these datasets can be utilized to limit the region of rainfall retrievals.

5) RAIN AND SNOW-COVER SEPARATION

In certain instances, a serious problem occurs in trying to separate rain from snow-covered ground. These situations occur when light rain is falling over cold ground, during the spring melt season when the snow pack melts during the day but refreezes during the night, and when strong convective rain occurs. These three situations are addressed below.

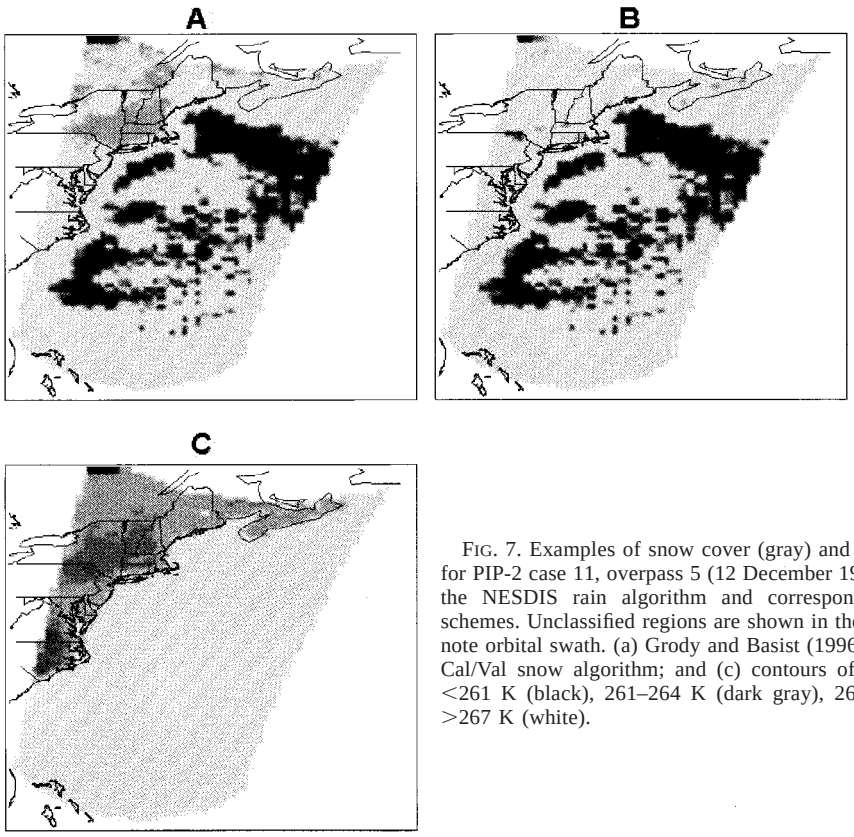

FIG. 7. Examples of snow cover (gray) and rain (black) detection for PIP-2 case 11, overpass 5 (12 December 1992, 1410 UTC) using the NESDIS rain algorithm and corresponding snow detection schemes. Unclassified regions are shown in the lightest shade to denote orbital swath. (a) Grody and Basist (1996) snow algorithm; (b) Cal/Val snow algorithm; and (c) contours of TB(22V) over land: $<$261 K (black), 261–264 K (dark gray), 264–267 K (gray), and $>$267 K (white).

(i) Separation under ''normal'' conditions

Based on the different surface temperatures that both of these surfaces exist, a simple threshold condition developed by Grody (1991) can be used to identify rain from snow. Whenever the TB(22V) $>$ 264 K, rain is present, provided that a scattering signal exists. This condition assumes that the surface is colder for snow conditions than in the case of rain. The threshold condition also works because the large ice crystals within the snow pack scatter at low frequencies, while the smaller-sized ice particles associated with light to moderate rain produces little scattering. This condition also identifies and removes cold, barren surfaces that scatter such as the Tibetan Plateau.

The 264-K threshold represents average conditions and the local value can deviate by approximately ± 3 K depending on the surface and atmospheric conditions. For example, cold rain can reduce the TB(22V) to 261 K while melting snow increases TB(22V) to 267 K. The problem is compounded for winter storm systems, where snow and rain generally fall adjacent to one another, as was the situation for PIP-2 case 11 and many of the cases examined during AIP-2 (see Negri et al. 1995). The GSCAT2 approach to this problem is to label observations near this threshold as ambiguous and introduce another check that examines the standard deviation of the TB(85H) in a 5×5 set of pixels centered around the pixel in question. Low values of this parameter indicate likely snow, while high values indicate convective rain (as described in section 3e(5)ii).

Shown in Fig. 7c are various temperature categories of the TB(22V). In this case, the region of ''possible snow'' depicted is a rather large region from central Pennsylvania and to the north and east, which was rather close to the actual snow cover at that time. Colder temperatures are evident farther south over Virginia and North Carolina, in a colder and drier air mass. However, since no scattering signature was present, no snow would be retrieved (e.g., Fig. 7a).

(ii) Convective storms and deep snow

For intense convective rain, which contains large ice particles, scattering occurs at low frequencies for both rain and snow. This can cause the TB(22V) to fall below 264 K. However, this confusion can easily be eliminated by applying the threshold under cold seasons and over certain latitude zones (i.e., the use of climatological limits of snow). However, a second condition is necessary to separate intense rain from snow cover (Grody 1991) and is given by

$$\mathrm{TB(22V)} > 175 + 0.49\mathrm{TB(85V)}. \qquad (9)$$

Failure to limit the use of this check as a function of

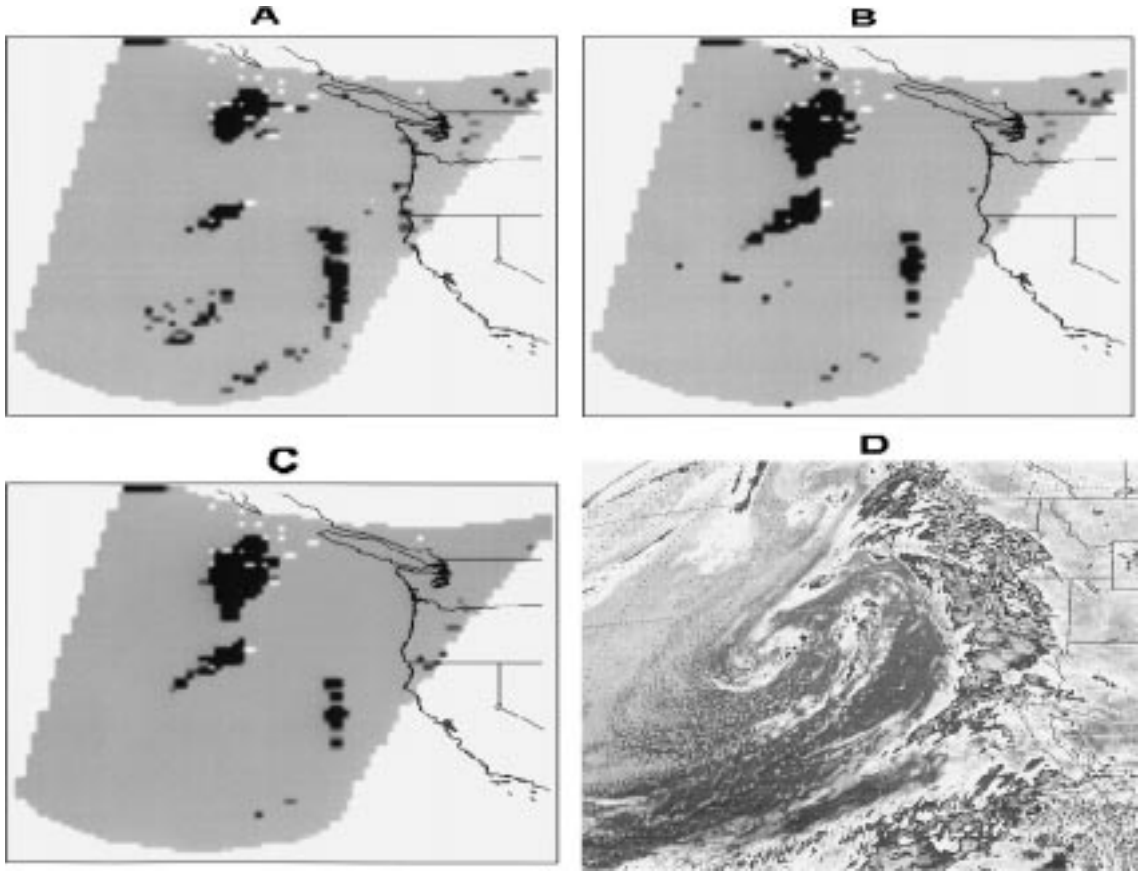

FIG. 8. Examples of ocean rain (black) detection for PIP-2 case 10, overpass 3 (12 February 1992, 1424 UTC). (a) Scattering index (Ferraro et al. 1994b), (b) values of liquid water (Weng and Grody 1994) in excess of 0.20 mm, (c) Cal/Val algorithm, and (d) GOES IR enhanced image at 1301 UTC.

latitude and season could eliminate some pixels in intense convective systems. As previously described, the GSCAT2 method would classify these situations as rain if the standard deviation of the TB(85H) measurements of adjacent pixels is large.

(iii) Refrozen snow

In the Northern Hemisphere during spring months (March–June), there tends to be large regions of melting snow that refreezes at night and continues to be a strong scatterer at 85 GHz but becomes misclassified as rain. It is speculated that warmer and moister atmospheric and surface conditions in the spring may be the cause of an increase in TB(22V), so that this threshold needs to be increased in order to properly separate rain and refrozen snow. This misclassification predominates in the evening data, when surface temperatures are warm and the daily melting process is large. To eliminate these melting snow conditions during the daytime overpasses, use of a 267-K threshold for TB(22V) in conjunction with Eq. (9) will generally work and was adopted by Ferraro et al. (1996) for use in the rainfall product delivered to the GPCP, when applied with various latitudinal limits during the months of January through June. However, this will eliminate some cold rain pixels.

f. Ocean surface screens

1) RAIN IDENTIFICATION

Rain identification over ocean can be accomplished through both scattering and emission-based methods. Many of these are detailed in Smith et al. (1998). Obviously, the validation of such techniques becomes difficult over open ocean where little or no validation data exist. Recent use of ship reports to evaluate the occurrence of rainfall retrieved by the SSM/I provides some insight as to which techniques perform best in certain rainfall regimes (Petty 1995).

Some of the simpler methods that can be used as a first guess of the rain–no rain boundary include the scattering index approach (e.g., Ferraro et al. 1994b), attenuation-based tests (e.g., Hollinger 1991), and the emission approach (e.g., Weng and Grody 1994). Examples of the use of these techniques are shown in Fig. 8 (PIP-2 case 10, overpass 1), which depicts a complex

winter low pressure center approaching the west coast of the United States.

All three approaches presented in Fig. 8 identify the main areas of precipitation. Both the attenuation-based (Fig. 8b) and emission approach (Fig. 8c) show almost the same regions of rain and a larger extent of rain than the scattering approach (Fig. 8a). This is not surprising since they rely on information from the 37-GHz channels, which is more sensitive to light rain. Note, however, that the scattering-based method shows some small areas of rain in the south central portion of the swath that is not detected by the other two methods. These are small-scale cellular convective showers related to the upper-level low feature (see GOES IR image in Fig. 8d), which contain ice aloft and either cannot be resolved by the larger FOVs at 37 GHz or contain small amounts of liquid water due to a very low freezing level height.

2) SEA ICE

As was the case for snow cover, sea ice can be detected via dynamic or climatological approaches. The Cal/Val algorithm (Hollinger 1991) is a complex set of tests to determine ice concentration and type. Using the oceanic scattering index derived by Ferraro et al. (1994b), sea ice is detected when this threshold exceeds 10 K. To separate and remove sea ice from all but the heaviest precipitation, apply the condition

$$\mathrm{TB(22V)} < 44 + 0.85\mathrm{TB(19V)}. \quad (10)$$

This relationship accounts for all types of sea ice (e.g., new and multiyear), including partially filled ice within the 19-GHz footprint. A second check is used to separate sea ice from heavy precipitation and is given by

$$\mathrm{TB(22V)} > 264 \quad \text{and} \quad \mathrm{TB(22V)} - \mathrm{TB(19V)} < 2. \quad (11)$$

Care must be taken to only apply this check to mid- and high-latitude regions or where the FNMOC surface tag identifies the footprint as possible or permanent ice.

The FNMOC tag includes categories for possible ice and permanent ice, both based upon climatologies. NASA has recently published an atlas of sea ice parameters based upon SMMR and SSM/I (Gloersen et al. 1992) while Ferraro et al. (1996) have produced one based upon SSM/I. All of these climatologies can be used to mask regions where rain retrievals are not possible.

3) NONRAINING CLOUDS

A problem exists in properly identifying clouds that are producing rain from those that are not. Defining a threshold that works in every climatic regime is extremely difficult, since there is very little validation data available. This is because the SSM/I measures the integrated volume of liquid in the FOV, which is a function of cloud droplet size and density, cloud thickness, freezing level, cloud base height, and depth of the rain layer. This is probably the single most reason of the wide range of results found over the ocean during PIP-1 and PIP-2.

Although there is no specific screen that can be reliably used to separate nonraining and raining clouds, thresholds can be selected that can be either very liberal (i.e., detect the lightest rains at the expense of misclassifying nonraining clouds) or very conservative (i.e., detect only rain above a certain threshold at the expense of eliminating light rain pixels). Figure 9 shows examples of applying different liquid water thresholds to the Weng and Grody (1994) algorithm. A GOES IR image is also provided for comparison purposes.

4) SURFACE WINDS

As was previously discussed, strong winds near the ocean surface impacts the emitting temperature and polarization signature, especially at the lower frequencies. Depending on the nature of the retrieval algorithm, this can cause significant misclassification of the area of rain where no rain is present. Most susceptible are algorithms that rely on simple TB thresholds to identify areas of rain. This effect is most likely to take place at the mid- and high-latitude regions, especially in the winter season. Clearly, the use of wind speed retrieval algorithms (e.g., Goodberlet 1989) should be used in conjunction with the rain retrievals, especially those which rely on lower frequencies and polarization differences. For example, this wind speed algorithm is used in the retrieval technique described by Petty (1994a,b).

5) "COLD" OCEAN

Under clear, calm conditions, the ocean surface emissivity is at its lowest (Fig. 1). If the atmosphere is dry, extremely low TBs are found. These can pose a serious problem to some retrieval algorithms, especially those 85-GHz scattering-based techniques that use single polarization temperature thresholds to delineate rain areas and retrieve rain rate. An empirically derived test developed by Adler et al. (1993) for use with the GSCAT2 algorithm identifies these regions as

$$\mathrm{TB(85H)} - \mathrm{TB(37H)} > 3 \quad \text{and} \quad \mathrm{TB(37H)} < 190\ \mathrm{K}. \quad (12)$$

4. Strengths and weaknesses of current screening approaches

As has been detailed so far in this paper, there are a variety of approaches that can be used to accurately detect rain areas and other similar signatures from each other. Some of the techniques are rather easy to implement while others are more sophisticated and involve detailed programming logic to implement correctly. The techniques most appropriate for use on a global scale

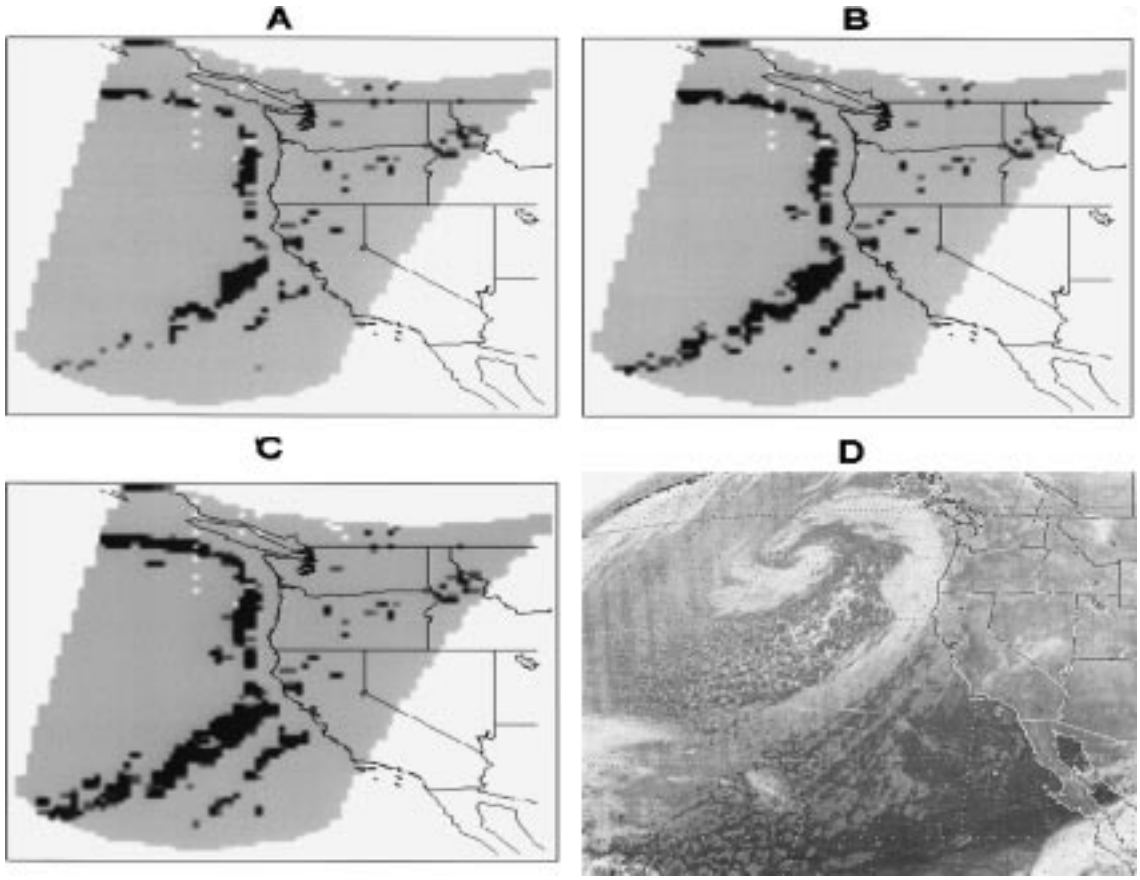

FIG. 9. Impact of varying the liquid water threshold to delineate regions of rain (black) from clouds for PIP-2 case 10, overpass 3 (14 February 1992, 1358 UTC). The algorithm of Weng and Grody (1994) is used. (a) 0.25 mm threshold, (b) 0.20 mm threshold, (c) 0.15 mm threshold, and (d) GOES IR image from 13:31 UTC.

are somewhat a function of the precipitation algorithm being employed and involve trade-offs concerning the detection of light rain. Also, computation time is a consideration, especially for operational rainfall retrievals.

Table 1 summarizes the status of screens for each of the categories presented in the paper and is intended to give some impression on the maturity of these algorithms. In addition, some of their advantages and disadvantages are presented.

5. A procedure for developing a common rain/no rain identification screen

a. Overview

An advantage of a robust independent rainfall screen is that a group of algorithms, ranging from very simple empirical approaches to complex physically based schemes, all equipped with the same screening procedure, can be compared on the basis of a common set of raining pixels. One of the problems in isolating differences between precipitation algorithms is that there are two general sources of differences, one due to the conversion of TBs to rain rates (RRs), the other due to differences in which pixels are designated as raining by the various algorithms. In order to facilitate a comparison between the wide variety of PIP-2 algorithms in which screen differences were inhibited, and also to isolate purely differences associated with the TB-RR conversion, a common screening procedure was invoked based on the fine-tuning of the land–ocean screening procedure of Ferraro et al. (1994b), including a modification to the ocean component. The modification, which is a 19–37-GHz liquid water emission test based on the study of Weng and Grody (1994), and is now part of the current NESDIS operational algorithm (Ferraro and Marks 1995), provides a more thorough check on the possibility that pixels contain rain if an initial check fails, based strictly on detection of the rain-induced scattering signature at 85 GHz. The details of how the common screening approach is used to isolate algorithm differences in the PIP-2 intercomparison analysis are provided in the studies of Smith et al. (1998) and Smith and Mugnai (1997, manuscript submitted to *J. Atmos. Sci.*).

b. Methodology

The technique used to create a common screening algorithm that incorporates a portion of the PIP-2 val-

TABLE 1. Summary of screening techniques. Maturity ranges from 1 (low) to 5 (high).

Parameter	Maturity	Strengths	Weaknesses
Data QC	5	Wentz data fairly ''clean'' Other methods viable	Screens may be difficult to use in operational environment
Geographic screen	4	Improve coastline retrievals	Somewhat computer expensive
Land: rain/no rain	3	Warm season rains Easy to use	Cold season rains Confusion with other scattering surfaces
Deserts	3	Identifies most large-scale zones Easy to implement	Limited to certain desert types Not well-tested globally
Semiarid land	2	Identifies large-scale zones Easy to implement	Can remove light rain regions Not well-tested globally
Snow cover	4	Dry and refrozen snow Rather easy to implement Climatologies available	Melting snow Cold desert regions Can be difficult to separate from rain
Ocean: rain/no rain	3	All rain types Some simple approaches	Rain-rate threshold an issue Regional differences Separation from clouds an issue
Sea ice	5	Well-studied product Climatologies available	Confusion with rain Best algorithms complicated
Ocean surface wind	3	Several algorithms available Easy to implement	Primarily for nonraining FOV Not needed for all algorithms Impact on raining FOVs unclear
Clear, calm ocean	4	Easy to implement	Tuned for low to midlatitudes

idation data, specifically radar validation data scenes from 36 of the 118 PIP-2 case–overpass events representing a selection of different locations, meteorological situations, years, and days of the year is described below. The main criterion for selecting overpasses used in the common screen analysis was that the radar dataset for a given event consisted of a relatively large range of rain rates over a meteorologically recognizable feature within a given storm system. Since not all of the PIP-2 case–overpass events included validation data, and not all of those that did included radar data (some validation scenes were developed from rain gauge data), only a subset of the original events were useful for this analysis. Moreover, of the subset of events that consisted of radar data, some events were either too restricted in their coverage of the given storm or exhibited too little variability in the rain rates across the validation scene. A detailed description of the PIP-2 case–overpass events is given in Smith et al. (1998). The specific case (Ca)–overpass (Op) events used for the screen analysis area:

1) Ca01Op01; 2) Ca02Op01; 3) Ca04Op01;
4) Ca04Op03; 5) Ca05Op01; 6) Ca05Op03;
7) Ca05Op06; 8) Ca05Op07; 9) Ca06Op05;
10) Ca06Op06; 11) Ca06Op07; 12) Ca08Op01.
13) Ca09Op03; 14) Ca09Op05; 15) Ca09Op07;
16) Ca09Op09; 17) Ca09Op10; 18) Ca09Op11;
19) Ca12Op01; 20) Ca12Op05; 21) Ca13Op01;
22) Ca13Op02; 23) Ca13Op05; 24) Ca14Op01;
25) Ca16Op01; 26) Ca17Op01; 27) Ca19Op01;
28) Ca19Op03; 29) Ca19Op04; 30) Ca21Op06;
31) Ca22Op03; 32) Ca23Op02; 33) Ca25Op05;
34) Ca25Op09; 35) Ca26Op03; 36) Ca28Op04.

The common screen was developed using variational analysis in which specific parameters of the Ferraro et al. (1994b) screen, which were known to be dependent on the training dataset, were tuned according to the selected PIP-2 radar dataset. In this analysis, five such parameters were tuned for the ocean screen, while five different parameters were tuned for the land screen. Since the radar data had been mapped into cells equivalent to those of the high-resolution SSM/I brightness temperature scenes, the one-to-one relationship between radar pixels and TB pixels was straightforward. The radar pixels were treated as a binary entity, that is, either indicating YES (Y) for rain or NO (N) for no rain. In the variational analysis, the optimized cost function is based on the Heidke skill score (SSH) of the binary truth table determined by cross-tabulating the N or Y radar-rain designators with the screen-based rain designator. The Heidke skill score of a binary truth table is given by the sum of the joint frequencies of the two diagonal elements (NN + YY), over the total sample (NT = NN + YN + NY + YY), adjusted by a correction term (E) that penalizes the score according to the joint frequencies of the off-diagonal elements

$$(E = \{[NN + YN] \times [NN + NY] + [NY + YY] \times [YN + YY]\}/NT).$$

Therefore, SSH = (NN + YY − E)/(NT − E). In tuning the screening coefficients, SSH was maximized over the allowable ranges of variation in the tunable parameters, first for the ocean screen, then for the land screen. In the subset of 36 case–overpass radar scenes used for the ocean analysis, 28 of them contained ocean pixels. A

total of 5132 over-ocean pixels were involved. In the case of the land analysis, a total of 11 037 pixels were involved derived from 32 separate case–overpass events.

1) OCEAN

In mathematical terms, the ocean screen is invoked by first synthesizing a scattering-free TB(85V) emission signature (85VE) from a regression expression using low-frequency TBs [following Grody (1991) and Ferraro et al. (1994b)]:

$$85\text{VE} = -174.4 + 0.715\,\text{TB}(19\text{V}) + 2.439\,\text{TB}(22\text{V}) - 0.00504\,\text{TB}(22\text{V})^2. \quad (13)$$

As previously described, the scattering index (SI85) is then expressed by differencing the synthetic quantity with the measured quantity, i.e., SI85 = 85VE − 85V. If SI85 is less than or equal to a specified threshold TSI-O (nominally set to 10 K), then the pixel is assumed to contain no scattering-sized hydrometeors, although a further emission check is made for rain in this event. If this index is greater than TSI-O, signifying that scattering has depressed the TB(85V) over its purely emission magnitude, then the pixel scene is assumed to contain some type of liquid and/or frozen precipitation, or possibly sea ice. Sea ice, which also produces a scattering signature, is differentiated from rain in a double discriminant test. The first checks if TB(22V) falls to the right of a discriminant line described by (10). The second check, described in (11), checks if TB(22V) is greater than a fixed threshold T22V-O (nominally 264 K) and if at the same time the TB(22V) − TB(19V) difference is less than a small positive value TBDIF (nominally 2 K). If either check is true, then sea ice is assumed present instead of rain. As shown in the Grody (1991) analysis, rain and sea ice are virtually differentiated by these threshold lines on a TB(19V) − TB(22V) diagram. If the scattering test fails to indicate rain, an alternate pair of emission checks are invoked, one at 19 GHz, the other at 37 GHz. These tests basically involve testing if liquid water paths (LWPs), formulated from both a combination of TB(19V) and TB(22V), and TB(37V) and TB(22V), reach critical thresholds. The first test involving TB(19V) can be viewed as a test for moderate to heavy rain in which a TB(37V) would be saturated; the second involving TB(37V) is for light rain in which a TB(19V) would exhibit too little dynamic range. The liquid water formulations (in kg m^{-2} or mm), which are empirical expressions following Weng and Grody (1994), are

$$\text{LWP}(19) = -2.70[\ln(290 - 19\text{V}) - 2.84 - 0.4\,\ln(290 - 22\text{V})] \quad (14a)$$

$$\text{LWP}(37) = -1.15[\ln(290 - 37\text{V}) - 2.99 - 0.32\,\ln(290 - 22\text{V})]. \quad (14b)$$

For the 19-GHz test, if LWP(19) exceeds a threshold, TLWP19 (nominally 0.6 kg m^{-2}), then rain is assumed present; at 37 GHz, if LWP(37) exceeds a corresponding threshold, TLWP37 (nominally 0.2 kg m^{-2}), then rain is assumed present. Therefore, if the scattering test fails to indicate rain but either of the LWP tests are positive, rain is assumed present, and by virtue of testing at both 37 and 19 GHz, the emission screen is responsive to a wide range of rain conditions.

2) LAND

For the land case, an equivalent scattering index test is made for rain (in which the scattering index threshold TSI-L is nominally set to 10 K). However, as previously described, possible conflicts exist due to surfaces such as snow cover, desertified regions, or cold semiarid regions, all of which exhibit significant scattering signatures. Following the formulation of Grody (1991) previously described, snow cover can be differentiated from precipitation with a discriminant test between TB(22V) and TB(85V) [e.g., Eq. (9)] and a check to test if the TB(22V) TB falls below a specified threshold T22V-L (nominally 264 K). The desert test is a simple 19-GHz polarization check [e.g., Eq. (4)], in which if the TB(19V) − TB(19H) difference exceeds a specified degree of polarization threshold, T19DP1 (nominally 20 K), then the scattering is assumed to have been produced by a nonvegetated surface. Finally, the tests described in (6) are used for identifying semiarid regions. In this case, a smaller degree of polarization threshold T19DP2 is used (nominally 7 K), but, to ensure that the scene is not rain with some residual 19-GHz polarization, a simultaneous check of TB(85V) is made to determine if it is above a threshold T85V-L, beyond which rain is unlikely (nominally 253 K).

3) DERIVATION OF THE SCREENS

The above screen descriptions identified five tunable ocean screen parameters, 1) TSI-O, 2) TLWP19, 3) TLWP37, 4) T22V-O, and 5) TBDIF, and five tunable land screen parameters, 1) TSI-L, 2) T22V-L, 3) T19DP1, 4) T19DP2, and 5) T85V-L, along with the nominal values used in the current operational NESDIS algorithm. During the tuning procedure, the variational analysis altered several of these parameters, although not all of them. Table 2 indicates both nominal values and final values relative to the 36 PIP-2 case–overpasses. As can be seen, the tuning procedure acted to increase the thresholds of most of the parameters, indicating that perhaps the nominal values in the NESDIS algorithm detected too much of an area of rain when compared with the 36 cases used in the tuning procedure.

TABLE 2. A description and summary of a set of SSM/I screening parameters. The parameters are described in the text. The nominal values refer to those used in the NESDIS algorithm, while the derived values refer to those obtained from the variational analysis.

Surface	Parameter	Nominal value	Derived value
Ocean	TSI-O	10 K	13 K
	TLWP19	0.6 kg m^{-2}	0.6 kg m^{-2}
	TLWP37	0.2 kg m^{-2}	0.3 kg m^{-2}
	T22V-O	264 K	264 K
	TBDIF	2 K	2 K
Land	TSI-L	10 K	11 K
	T22V-L	264 K	264 K
	T19DP1	20 K	23 K
	T19DP2	7 K	9 K
	T85V-L	253 K	253 K

6. Summary

This paper has presented a description and summary of SSM/I screening techniques that can be used to identify and remove surface artifacts from rain retrievals. Besides the issue of surface screens, the study also considered the problem of coastline identification and methods to validate the quality of brightness temperature measurements. Where possible, more than one method was discussed, and examples on its use were presented through application with actual SSM/I case studies used in PIP-2. Trade-offs between the complexity and the effectiveness of each screening technique, as well as their strengths and weaknesses, were also discussed. Finally, a summary on the design of a common screen for use in the PIP-2 intercomparison analysis was described.

Although many of the screens that were presented appear simple in formulation and stem from empirical analysis, one cannot underestimate their importance nor their physical significance. The failure to properly identify and remove surface artifacts from the retrievals of a given algorithm will ultimately lead to the discrediting of that algorithm, especially when used to generate global monthly rainfall estimates, particularly those deemed suitable for climatic studies.

The complicated interaction of earth-emitted microwave radiation with various surface types and atmospheric variables makes the development of surface screens that work everywhere very difficult. Hence, the designs of global screens are conservative in nature and may involve incorrectly removing some raining pixels in certain regions during certain meteorological situations. Certainly, the detection of light rain and the entire question of the threshold of detectibility of light rain remains as a problem in research. On the regional scale, we submit that better screens can likely be developed and better tuned for a wider range of conditions. However, it also remains as a research problem to determine if such improvements will be significant without first advancing the measurement technology.

Acknowledgments. The authors are grateful to James Dodge and his colleagues at NASA, who conceived the WetNet Project, made it an overwhelming success, brought together researchers throughout the world, and ultimately provided us with the opportunity to contribute to this special issue. The lead author (RF) also acknowledges Eric Smith for his dedicated effort in PIP-2 and encouraging the collaborative effort on the common screen. RF also thanks all the co-authors for their contributions to the manuscript; it was truly a ''team effort''! Finally, RF also wants to express sincere gratitude to Norm Grody, who is truly the ''expert'' in this area of research and has taught me most of what I know in this field.

REFERENCES

Adler, R. F., A. J. Negri, P. R. Keehn, and I. M. Hakkarinen, 1993: Estimation of monthly rainfall over Japan and surrounding waters from a combination of low-orbit microwave and geosynchronous IR data. *J. Appl. Meteor.,* **32,** 335–356.

——, G. J. Huffman, and P. R. Keehn, 1994: Global tropical rain estimates from microwave-adjusted geosynchronous IR data. *Remote Sens. Rev.,* **11,** 125–152.

Arkin, P. A., and P. Xie, 1994: The Global Precipitation Climatology Project: First algorithm intercomparison project. *Bull. Amer. Meteor. Soc.,* **75,** 401–419.

Barrett, E. C., J. Dodge, H. M. Goodman, J. Janowiak, C. Kidd, and E. A. Smith, 1994a: The first WetNet precipitation intercomparison project (PIP-1). *Remote Sens. Rev.,* **11,** 49–60.

——, and the Entire PIP-1 Investigation Team, 1994b: The first WetNet precipitation intercomparison project (PIP-1): Interpretation of results. *Remote Sens. Rev.,* **11,** 303–373.

Berg, W., and R. Chase, 1992: Determination of mean rainfall from the special sensor microwave/imager (SSM/I) using a mixed lognormal distribution. *J. Atmos. Oceanic Technol.,* **9,** 121–141.

Chang, A. T. C., L. S. Chiu, and T. T. Wilheit, 1993: Oceanic monthly rainfall derived from SSM/I. *Eos, Trans. Amer. Geophys. Union,* **74,** 505–513.

Conner, M. D., and G. W. Petty, 1996: SSM/I brightness temperature deviations from gridded monthly means as a basis for over-land precipitation estimation. Preprints, *Eighth Conf. on Satellite Meteorology and Oceanography,* Atlanta, GA, Amer. Meteor. Soc., 295–298.

Ferraro, R. R., and G. F. Marks, 1995: The development of SSM/I rain-rate retrieval algorithms using ground-based radar measurements. *J. Atmos. Oceanic Technol.,* **12,** 755–770.

——, N. C. Grody, and J. A. Kogut, 1986: Classification of geophysical parameters using passive microwave satellite measurements. *IEEE Trans. Geosci. Remote Sens.,* **24,** 1008–1013.

——, ——, D. Forsyth, R. Carey, A. Basist, J. Janowiak, F. Weng, G. Marks, and R. Yanamandra, 1994a: Microwave measurements produce global climatic, hydrologic data. *Eos. Trans. Amer. Geophys. Union,* **75,** 337–343.

——, ——, and G. F. Marks, 1994b: Effects of surface conditions on rain identification using the SSM/I. *Remote Sens. Rev.,* **11,** 195–209.

——, F. Weng, N. C. Grody, and A. Basist, 1996: An eight-year (1987–1994) time series of rainfall, clouds, water vapor, snow-cover, and sea-ice derived from SSM/I measurements. *Bull. Amer. Meteor. Soc.,* **77,** 891–905.

Gloersen, P., W. J. Campbell, D. J. Cavalieri, J. C. Comiso, C. L. Parkinson, and H. J. Zwally, 1992: Arctic and Antarctic sea ice, 1978–1987: Satellite passive-microwave observations and analysis. NASA SP-511, 290 pp. [Available from NASA, Scientific and Technical Information Program, Washington, DC 20546.]

Goodberlet, M. A., C. T. Swift, and J. C. Wilkerson, 1989: Remote

sensing of ocean surface winds with the special sensor microwave/imager. *J. Geophys. Res.,* **94,** 14 547–14 555.

Grody, N. C., 1988: Surface identification using satellite microwave radiometer. *IEEE Trans. Geosci. Remote Sens.,* **26,** 850–859.

——, 1991: Classification of snow cover and precipitation using the Special Sensor Microwave/Imager (SSM/I). *J. Geophys. Res.,* **96,** 7423–7435.

——, and A. Basist, 1996: Global identification of snow cover using SSM/I measurements. *IEEE Trans. Geosci. Remote Sens.,* **34,** 237–249.

Hollinger, J., 1991: DMSP SSM/I calibration/validation. Naval Research Laboratory Final Rep. Parts I & II, 419 pp. [Available from Naval Research Laboratory, Washington, DC 20375-5000.]

Kniveton, D. R., B. C. Motta, H. M. Goodman, M. Smith, and F. J. LaFontaine, 1994: The first Wetnet precipitation intercomparison project: Generation of results. *Remote Sens. Rev.,* **11,** 243–302.

Lure, Y. M. F., N. C. Grody, Y. S. P. Chiou, and H. Y. M. Yeh, 1993: Data fusion with neural networks for classification of earth surface from microwave satellite measurements. *Telem. Informatics,* **10,** 1–10.

NASA, cited 1996: NOAA-NASA pathfinder land products data sets. [Available on-line from http.//wwwdaac.msfc.nasa.gov/userservices/ pathfdr_land_products_readme.html.]

Neale, C. M. U., M. J. McFarland, and K. Chang, 1990: Land surface classification using microwave brightness temperatures from the Special Sensor Microwave/Imager. *IEEE Trans. Geosci. Remote Sens.,* **28,** 829–838.

Negri, A. J., E. J. Nelkin, R. F. Adler, G. J. Huffman, and C. Kummerow, 1995: Evaluation of passive microwave precipitation algorithms in wintertime midlatitude situations. *J. Atmos. Oceanic Technol.,* **12,** 20–32.

Petty, G. W., 1994a: Physical retrievals of over-ocean rain rate from multichannel microwave imagery. Part I: Theoretical characteristics of normalized polarization and scattering indices. *Meteor. Atmos. Phys.,* **54,** 79–99.

——, 1994b: Physical retrievals of over-ocean rain rate from multichannel microwave imagery. Part II: Algorithm implementation. *Meteor. Atmos. Phys.,* **54,** 101–121.

——, 1995: Frequencies and characteristics of global oceanic precipitation from shipboard present-weather report. *Bull. Amer. Meteor. Soc.,* **76,** 1593–1616.

Schmugge, T. J., 1983: Remote sensing of soil moisture: Recent advances. *IEEE Trans. Geosci. Remote Sens.,* **GE-21,** 336–344.

Smith, E., and A. Mugani, 1997: Strengths and weaknesses of current SSM/I rainfall retrieval algorithms. *J. Atmos. Sci.,* in press.

Smith, E. A., J. Lamm, R. Adler, J. Alishouse, K. Aonashi, E. Barrett, P. Bauer, W. Berg, A. Chang, R. Ferraro, J. Ferriday, S. Goodman, N. Grody, C. Kidd, D. Kniveton C. Kummerow, G. Liu, F. Marzano, A. Mugnai, W. Olson, G. Petty, A. Shibata, R. Spencer, F. Wentz, T. Wilheit, and E. Zipser, 1998: Results of the WetNet PIP-2 project. *J. Atmos. Sci.,* **55,** 1483-1536.

Spencer, R. W., 1993: Global oceanic precipitation from the MSU during 1979–1991 and comparisons to other climatologies. *J. Climate,* **6,** 1301–1326.

——, 1994: Oceanic rainfall monitoring with the microwave sounding units. *Remote Sens. Rev.,* **11,** 153–162.

——, H. M. Goodman, and R. E. Hood, 1989: Precipitation retrieval over land and ocean with the SSM/I. Part I: Identification and characteristics of the scattering signal. *J. Atmos. Oceanic Technol.,* **6,** 254–273.

Weng, F., 1992a: A multi-layer discrete-ordinate method for vector radiative transfer in a vertically-inhomogeneous, emitting and scattering atmoshpere—I. Theory. *J. Quant. Spectrosc. Radiat. Transfer,* **47,** 19–33.

——, 1992b: A multi-layer discrete-ordinate method for vector radiative transfer in a vertically-inhomogeneous, emitting and scattering atmoshpere—II. Application. *J. Quant. Spectrosc. Radiat. Transfer,* **47,** 34–42.

——, and N. C. Grody, 1994: Retrieval of cloud liquid water using the special sensor microwave imager (SSM/I). *J. Geophys. Res.,* **99,** 25 535–25 551.

Wentz, F. J., 1991: User's manual—SSM/I antenna temperature tapes (Revision 1) Remote Sensing Systems Tech. Rep. 120191, 70 pp. [Available from Remote Sensing Systems, 1101 College Ave., Suite 220, Santa Rosa, CA 95404.]

——, 1992: Final report production of SSM/I data sets. Remote Sensing Systems Tech. Rep. 090192, 78 pp. [Available from Remote Sensing Systems, 1101 College Ave., Suite 220, Santa Rosa, CA 95404.]

——, 1993: User's manual—SSM/I antenna temperature tapes (Revision 2). Remote Sensing Systems Tech. Rep. 120193, 34 pp. [Available from Remote Sensing Systems, 1101 College Ave., Suite 220, Santa Rosa, CA 95404.]

Wigneron, J., Y. Kerr, A. Chanzy, and Y. Jin, 1993: Inversion of surface parameters from passive microwave measurements over a soybean field, 1993. *Remote Sens. Env.,* **46,** 61–72.

Wilheit, T. T., A. T. C. Chang, M. S. V. Rao, E. B. Rodgers, and J. S. Theon, 1977: A satellite technique for quantitatively mapping rainfall rates over the oceans. *J. Appl. Meteor.,* **16,** 551–560.